Solid-State 45Sc NMR Studies of Cp*2Sc-X and Cp*2ScX(THF)

Journal:	*Dalton Transactions*
Manuscript ID	DT-ART-06-2018-002623.R2
Article Type:	Paper
Date Submitted by the Author:	17-Aug-2018
Complete List of Authors:	Huynh, Winn; University of California Culver, Damien; University of California Tafazolian, Hosein; University of California Conley, Matthew; University of California,

Solid-State ^{45}Sc NMR Studies of Cp*$_2$Sc–X and Cp*$_2$ScX(THF)

Winn Huynh,[†] Damien B. Culver,[†] Hosein Tafazolian and Matthew P. Conley*

Department of Chemistry, University of California, Riverside, California 92521, United States

ABSTRACT

Cp*$_2$Sc–X, where X is a halide, were synthesized and studied by solid-state ^{45}Sc NMR to determine how the Sc–X bond affects quadrupolar NMR parameters. The experimental quadrupolar coupling constants (C$_Q$) show that the fluoride has the largest coupling constant and that the iodide has the smallest coupling constant. DFT analysis of this data indicates that the C$_Q$ of these compounds is related to core scandium and halide orbitals, which is related to polarizability of the halide and the Sc–X distance. Cp*$_2$ScX(THF) were also investigated by solid-state ^{45}Sc NMR spectroscopy, and have much smaller C$_Q$ values than the base-free halides. This is related to the change in structure of the THF adduct and occupation of orbitals of π-symmetry that reduce C$_Q$.

Introduction

Solid-state NMR is a powerful method to obtain detailed information about structures of small molecules, proteins, and materials. Almost every element contains at least one active NMR nucleus, and almost all of these nuclei are quadrupolar (spin > ½). For example, scandium contains one NMR active nucleus (^{45}Sc, 100 % abundant, I = 7/2). Organoscandium complexes are active in σ-bond metathesis reactions,[1] hydromethylation of olefins,[2] olefin polymerization,[3] activation of CO,[4] and reduction of CO_2.[5] This limited list of reactions involving scandium suggest that solid-state ^{45}Sc NMR could be useful to study the structure and bonding in organoscandium complexes. Solid-state ^{45}Sc NMR has been used to study small molecules,[6] crystalline porous materials,[7] glassy solids,[8] organoscandium sites supported on oxides,[9] and to establish the β-agostic structure in Cp*$_2$Sc–Et.[10]

In contrast to isotropic spin ½ nuclei, quadrupolar nuclei contain a nonspherical distribution of positive charge. This anisotropic distribution of charge affects the lineshape of quadrupolar NMR signals, usually resulting in much broader signals than obtained for spin ½ nuclei. The quadrupolar interaction involves the electric quadupole (eQ) moment, characteristic of a given nucleus, and the electric field gradient (EFG) tensor. The EFG tensor is a measure of charge distribution at the quadrupolar nucleus that is related to the ligands or bonding partners surrounding the quadrupolar nucleus, and is a very sensitive reporter to changes in structure.[11]

The EFG is a second-rank tensor (V, eq 1), and the three principal components are ordered such that $|V_{33}| \geq |V_{22}| \geq |V_{11}|$. The EFG tensor is described by the quadrupolar coupling constant (C_Q), which depends on the magnitude of V_{33} (eq 2; e = point charge; Q = nuclear quadrupole moment; h = Plank's constant). The C_Q is typically on the order of MHz, which is far larger than several other common NMR interactions (J coupling, dipolar coupling, chemical

shift anisotropy, etc.). The magnitude of V_{33} depends on the symmetry of the molecular environment, perturbations of core orbitals, and population of valence bonding orbitals.

$$V = \begin{vmatrix} V_{11} & 0 & 0 \\ 0 & V_{22} & 0 \\ 0 & 0 & V_{33} \end{vmatrix} \quad (1)$$

$$C_q = \frac{e^2 Q V_{33}}{h} \quad (2)$$

In this study, solid-state ^{45}Sc NMR spectra of Cp*$_2$Sc–X and Cp*$_2$ScX(THF) (X = F, Cl, Br, I) were recorded to determine how the σ- and π-bonding interactions comprising the Sc–X bond affect C_Q. The halides were chosen because previous EPR and UV-vis studies of d^1 Cp*$_2$Ti–X showed that the Ti–X bond affects spectroscopic properties, resulting in a π-donor spectrochemical series (F > Cl > Br > I).[12] The combined solid-state ^{45}Sc NMR and DFT studies of Cp*$_2$Sc–X show that C_Q is related to core orbitals on Sc and X, as well as the σ-ScX bond; π-effects contribute less to C_Q. Cp*$_2$ScX(THF) have smaller C_Q than the base-free halides. This behaviour originates from changes in geometry at Sc, which results in occupation of the LUMO of the base-free halide upon coordination of THF.

Experimental Section

All manipulations were performed under an atmosphere of argon. Benzene-d$_6$ was purchased from Cambridge Isotope Laboratories and dried over sodium/benzophenone, distilled under vacuum and stored inside a glove box. All other solvents were purchased from Fisher Scientific. Pentane and toluene were dried over sodium/benzophenone, degassed and distilled under vacuum. Lithium bromide was purchased from Sigma Aldrich and dried at 160 ^{o}C under high vacuum prior to use. Dry lithium iodide was purchased from Sigma Aldrich and used without

further purification. Vinyl fluoride was obtained from PCR Research Chemicals, Inc. The synthesis of Cp*$_2$ScCl, Cp*$_2$ScMe and Cp*$_2$ScI was reported previously.[1a]

Synthesis of Cp$_2$ScF:* Benzene (~10 mL) was condensed into a flask containing Cp*$_2$Sc–Me (500 mg, 1.5 mmol) by vacuum transfer at -196°C. The pale-yellow solution was warmed to room temperature, and the solution was exposed to 1 atm of vinyl fluoride (10 mmol). The reaction mixture evolves to a golden color. The mixture was stirred for 1 h at room temperature, and the volatiles were removed in vacuo. The yellow solid was extracted with pentane (10 mL), filtered, and recrystallized from concentrated pentane solution at -20 °C, yielding pale yellow crystals of Cp*$_2$ScF (155 mg, 31 %). ^{1}H NMR (C$_6$D$_6$, 300 MHz): 1.90 (s, 30H, C$_5$Me$_5$), ^{45}Sc{^{1}H} NMR (C$_6$D$_6$, 72.9 MHz): 65.7 ppm, ^{19}F NMR (C$_6$D$_6$, 282.4 MHz): 59 ppm. Anal. Calcd. For C$_{20}$H$_{30}$ScF: C, 71.82; H, 9.06. Found: C, 71.50; H, 8.74.

Synthesis of Cp$_2$ScBr:* Toluene (30 mL) was added by cannula to a Schlenk tube containing Cp*$_2$Sc–Cl (294 mg, 0.74 mmol) and LiBr (80.2 mg, 1.6 mmol, 2.2 eq.). The reaction mixture was heated to 95°C and stirred under argon for 22 h. The reaction mixture was cooled to room temperature and toluene was removed under vacuum. Pentane (20 mL) was added to the yellow solid to produce a yellow solution and a white solid, which was removed by filtration. The clear yellow pentane solution was concentrated to ~ 7 mL and stored at –20 °C. Cp*$_2$ScBr precipitates as yellow X-ray quality crystals (211 mg, 64%). ^{1}H NMR (C$_6$D$_6$, 300 MHz): 1.89 (s, 30H, C$_5$Me$_5$), ^{45}Sc{^{1}H} NMR (C$_6$D$_6$, 72.9 MHz): 203.3 ppm. Anal. Calcd. For C$_{20}$H$_{30}$ScBr: C, 60.75; H, 7.66. Found: C, 60.55; H, 7.49.

Synthesis of Cp$_2$ScI:* Toluene (20 mL) was added by cannula to a Schlenk tube containing Cp*$_2$ScCl (169 mg, 0.482 mmol) and LiI (80.2 mg, 0.6 mmol, 1.2 eq.). The reaction mixture was

heated to 80°C and stirred under argon for 26 h. The reaction mixture was cooled to room temperature and toluene was removed in vacuo. Pentane (20 mL) was added to the yellow solid to produce a yellow solution and a white solid, which was removed by filtration. The clear yellow pentane solution was concentrated to ~ 7 mL and stored at –20 °C. Cp*$_2$ScI precipitates as yellow X-ray quality crystals (158 mg, 74%). ^{1}H NMR (C$_6$D$_6$, 300 MHz): 1.91 (s, 30H, C$_5$Me$_5$), ^{45}Sc{^{1}H} NMR (C$_6$D$_6$, 72.9 MHz): 256.9 ppm.

*General procedure for the synthesis of Cp*2ScX(THF):* A sample of Cp*$_2$Sc–X (100-200 mg) was weighed into a flask containing a Teflon tap. The flask was connected to a high vacuum line and evacuated. THF (~ 5 mL) was condensed to the flask at 77 K, and the mixture was warmed to room temperature. Cp*$_2$ScX(THF) precipitates from THF as beige powders. Excess THF was removed under vacuum and the solid was dried at room temperature. Yields are essentially quantitative. C$_6$D$_6$ solutions of Cp*$_2$ScX(THF) show signals for Cp*$_2$Sc–X and free THF in ^{1}H, ^{13}C, and ^{45}Sc NMR spectra.

NMR Experiments: Solution phase ^{1}H and Sc{^{1}H} Hahn echo NMR spectroscopy were carried out on an Avance Bruker 300, and the spectra were referenced to the NMR solvent residual peak or an external standard of 0.11M ScCl$_3$ in 0.11 M aqueous HCl solution (0.00 ppm) respectively. Solid state NMR spectra were recorded in 4 mm zirconia rotors on 14.1 T Bruker Neo-600 NMR or 9.4 T Bruker Avance III spectrometers. Static ^{45}Sc{^{1}H} NMR spectra were recorded with a Hahn-echo pulse sequence, with full echo detection ($\pi/2 - \tau - \pi - $ acq), using frequency stepped acquisition at low ν_{RF} field strengths.[13] Echo delays (τ) were set to 100 – 250 μsec. All analytical simulations of solid state spectra were performed in Topspin using Sola line shape analysis. 3QMAS NMR spectra were acquired using a z-filtered pulse sequence,[14] and processed using the

shearing function in Topspin. 1D slices were extracted in Topspin and fit using Sola lineshape analysis.

DFT Calculations: The geometries of $Cp*_2Sc–X$ (X = F, Cl, Br, I) were optimized with Gaussian 09 using the B3LYP functional[15] containing Grimme's D3 dispersion with Becke-Johnson damping.[16] Sc and X were described with the SDD basis set,[17] and all other atoms were represented with the 6-31G(d,p) basis set. $Cp*_2ScX(THF)$ were optimized at the same level of theory. NMR parameters were calculated with the geometry-optimized structures using B3LYP/DZ in the Amsterdam Density Functional (ADF).[18] NMR shielding was calculated using the GIAO method.[19] Relativistic scalar two component zero order regular approximation (ZORA)[20] was included for $Cp*_2ScBr$, $Cp*_2ScI$, $Cp*_2ScBr(THF)$ and $Cp*_2ScI(THF)$.[21] The calculated isotropic chemical shift was referenced to geometry-optimized $Sc(H_2O)_6^{3+}$ at the same level of theory, which was used previously to reference ^{45}Sc chemical shift calculations.[6,22] Contributions of Naturalized Localized Molecular Orbitals (NLMO) to C_Q were calculated using the B3LYP/DZ level of theory in ADF, with scalar relativistic ZORA for complexes with bromine and iodine. This decomposition analysis provides key information on how the core and valence orbitals contribute to C_Q. A more detailed discussion of this technique was described previously.[11a]

Results

The synthesis of $Cp*_2Sc–X$ begin from $Cp*_2Sc–Cl$,[1a] and are shown in Scheme 1. $Cp*_2Sc–Br$ and $Cp*_2Sc–I$ were prepared by anion metathesis of $Cp*_2Sc–Cl$ with LiX in toluene slurries at 80 $^{\circ}C$. The products were isolated as yellow crystalline solids in good yields. $Cp*_2Sc–F$ did not form under similar conditions in the presence of LiF or AgF, and reactions with slightly

soluble [NMe$_4$][F] led to intractable mixtures. However, the reaction of Cp*$_2$Sc–Me with vinyl fluoride results in the formation of propene and Cp*$_2$Sc–F in moderate yield. This reaction likely proceeds by insertion of vinyl fluoride into the Sc–Me bond, followed by rapid β-F elimination. β-halide elimination is common in transition metal alkyls.[23]
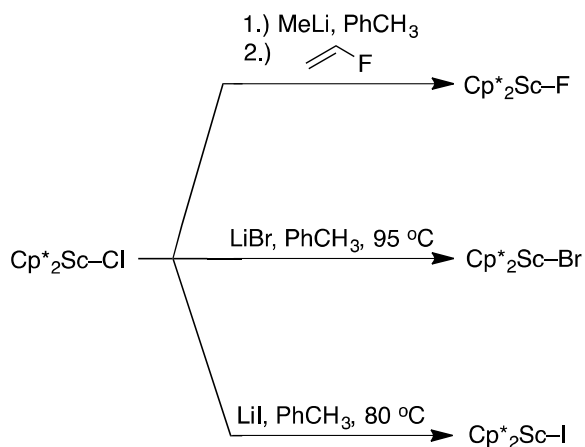
Scheme 1. Synthesis of Cp*$_2$Sc–X.

The solid-state structures of Cp*$_2$Sc–X are shown in Figure 1, and key structural parameters are summarized in Table 1. Cp*$_2$Sc–Cl crystallizes with four nearly identical molecules in the unit cell; the other halides crystallize with one molecule in the unit cell. Cp*$_2$Sc–X adopt typical bent C_{2v} structures expected for a d^0 metallocenes and are unremarkable. The Sc–X bond length of the Sc–X bond increases in the order F < Cl < Br < I, which is expected based on the differences in size of the halides.

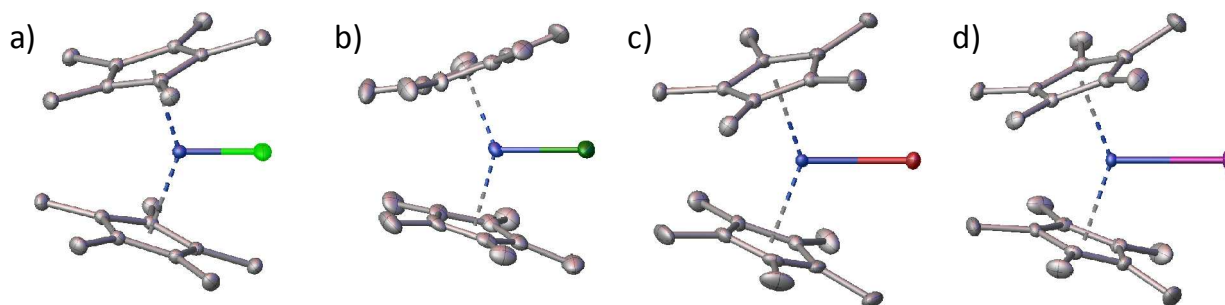**Figure 1.** X-ray crystal structures of Cp*$_2$Sc–F (a); Cp*$_2$Sc–Cl (b); Cp*$_2$Sc–Br (c); Cp*$_2$Sc–I (d).

Table 1. Selected distances (Å) and angles ($^{\circ}$) in Cp*$_2$Sc–X.

X	Cp*$_a$-Sc	Cp*$_b$-Sc	Cp*$_a$-Sc-Cp*$_b$	Sc-X	Cp*$_a$-Sc-X	Cp*$_b$-Sc-X
Sc–F	2.1648(101) Å	2.1630(132) Å	145.492(53)°	1.9274(12) Å	108.30	108.30
Sc–Cl[a]	2.1517(115) Å	2.1624(115) Å	142.713(240)°	2.4175(16) Å	108.57	109.45
Sc–Br	2.1630(131) Å	2.1648(98) Å	142.329(77)°	2.5840(3) Å	108.97	109.32
Sc–I	2.1630(132) Å	2.1648(131) Å	140.511(77)°	2.8194(3) Å	108.91	109.54

[a]– Average values for the four independent molecules in the unit cell, refer to the Supporting Information for details.

Cp*$_2$ScX(THF) were synthesized by suspending Cp*$_2$Sc–X in excess THF (eq 3), which results in rapid color change of the bright yellow Cp*$_2$Sc–X to form beige precipitates that are essentially insoluble in THF or hydrocarbon solvents. In C$_6$D$_6$ Cp*$_2$ScX(THF) form bright yellow solutions, and ^{1}H NMR spectra of these solutions contains signals for Cp*$_2$Sc–X and free THF, consistent with dissociation of THF from Cp*$_2$ScX(THF) in arene solvents. Attempts to obtain single crystals of Cp*$_2$ScX(THF) from saturated hydrocarbon solutions, or by slow

diffusion of THF onto hydrocarbon solutions of Cp*$_2$Sc–X were unsuccessful, resulting in microcrystalline solids unsuitable for X-ray diffraction analysis.

$$Cp*_2Sc–X \xrightarrow{\text{THF}} Cp*_2ScX(THF) \quad (3)$$

$$X = F, Cl, Br, I$$
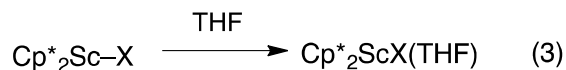
Solid-State NMR Studies

The static central transition solid-state ^{45}Sc NMR spectra of Cp*$_2$Sc–X at 14.1 T are shown in Figure 2. All show typical second order quadrupolar powder patterns. Qualitatively the fluoride has the broadest signal (~ 1100 ppm, ~ 160 kHz) while the other halides have similar spectral linewidths (~ 700 ppm, ~100 kHz) at this field strength. Simulations of these spectra are shown in red in Figure 2, and NMR parameters extracted from this data are summarized in Table 2. In addition to the C$_Q$ values extracted from the simulations of the spectra in Figure 2, values associated with the chemical shielding tensor, and the Euler angles associated with the orientations of these two tensors, are given in Table 2. The C$_Q$ values decrease in the order Cp*$_2$Sc–F (34.2 MHz) > Cp*$_2$Sc–Cl (30.0 MHz) ≈ Cp*$_2$Sc–Br (29.2 MHz) > Cp*$_2$Sc–I (27.4 MHz).
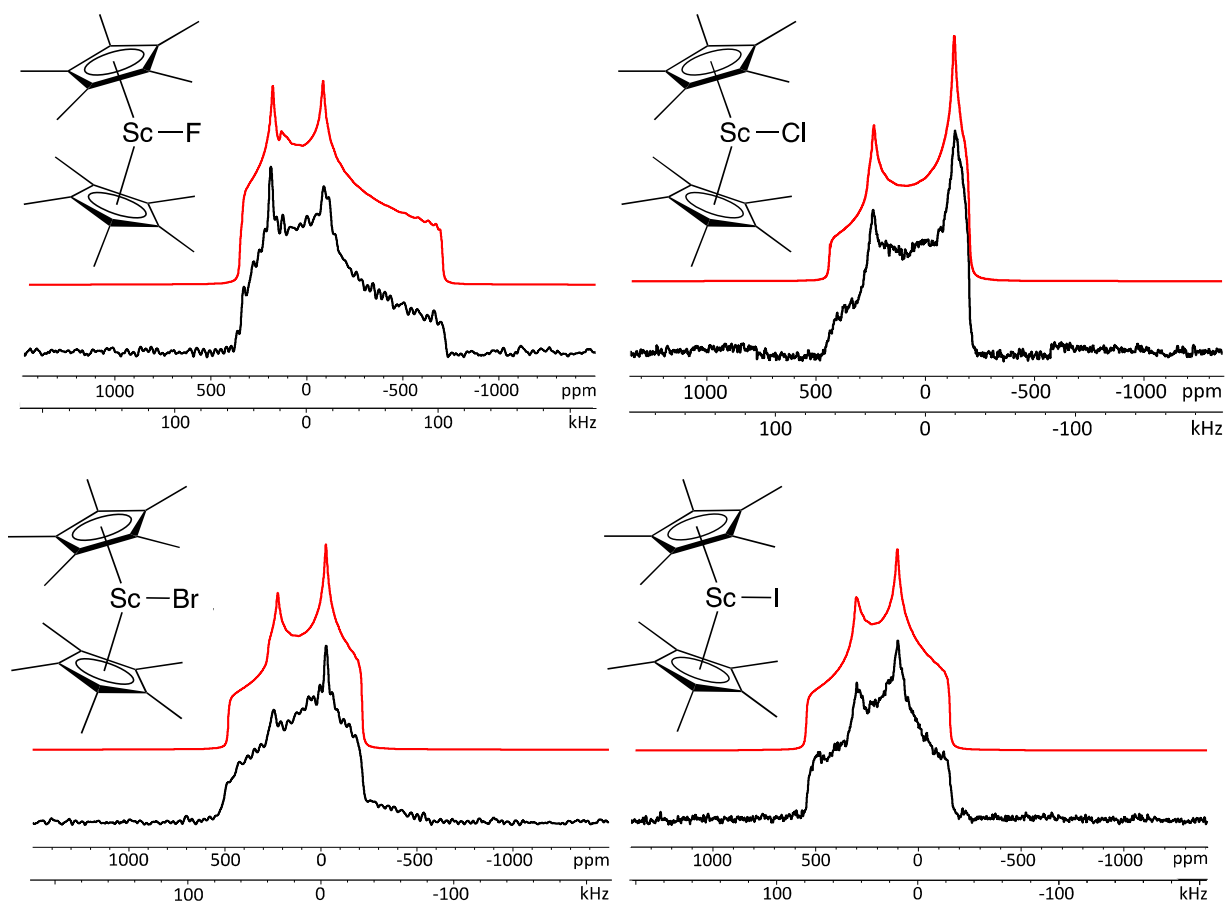
Figure 2. ^{45}Sc CT Solid-state NMR spectra of Cp*$_2$Sc–F (a); Cp*$_2$Sc–Cl (b); Cp*$_2$Sc–Br (c); Cp*$_2$Sc–I (d).

Table 2. ^{45}Sc NMR Parameters for Cp*$_2$ScX extracted from simulations in Figure 2.

X	δ_{iso} (ppm)	C_Q (MHz)	η	Ω (ppm)	κ	α (°)	β (°)	γ (°)
F	62	34.2	0.79	262	0.05	0	90	0

Cl	159	30.0	0.00	227	0.28	0	90	90
Br	201	29.2	0.11	235	0.88	0	90	0
I	266	27.4	0.29	176	0.44	0	90	0

The static solid state ^{45}Sc NMR data for Cp*$_2$ScX(THF) are summarized in Table 3. In all cases, Cp*$_2$ScX(THF) have significantly smaller C_Q values than their base-free counterparts. For example, Cp*$_2$ScF(THF) simulates as a single site giving a C_Q of 26.0 MHz (Figure S5), which is ~8 MHz smaller than the C_Q of Cp*$_2$Sc–F. The other halides result in complex static spectra that do not simulate as a single species. 2D NMR methods are useful in situations where multiple quadrupolar signals overlap in a static spectrum. The Multiple Quantum Magic Angle Spinning (MQMAS) 2D experiment provides high-resolution solid-state NMR spectra of half-integer quadrupolar nuclei. In MQMAS experiments triple-quantum transitions are excited by high power pulses, then reconverted to single-quantum coherences. Selection of the triple-quantum and single-quantum coherence evolution refocuses second-order quadrupolar interactions in the indirect dimension, resulting in a 2D spectrum that correlates second-order broadened quadrupolar signals to their isotropic chemical shifts.[24]

The results of the 3QMAS NMR spectrum for Cp*$_2$ScCl(THF) is shown in Figure 3a. Two peaks appear in the indirect dimension, indicating that two scandium sites are present in Cp*$_2$ScCl(THF). 1D projections of these sites shows that the C_Q are 7.5 and 7.3 MHz for these two sites, respectively (Table 3). These values that are significantly smaller than the C_Q of Cp*$_2$Sc–Cl (30.0 MHz). Figure 3b shows the simulated 1D ^{45}Sc MAS echo spectrum fit to C_Q obtained from the 3QMAS experiment, which fits the experimental data well. This fit is reproduced at 9.4 T (Figure S8). The C_Q values for Cp*$_2$ScBr(THF) and Cp*$_2$ScI(THF) were

determined using 3QMAS and 1D MAS spectra and are shown in the Supporting Information.
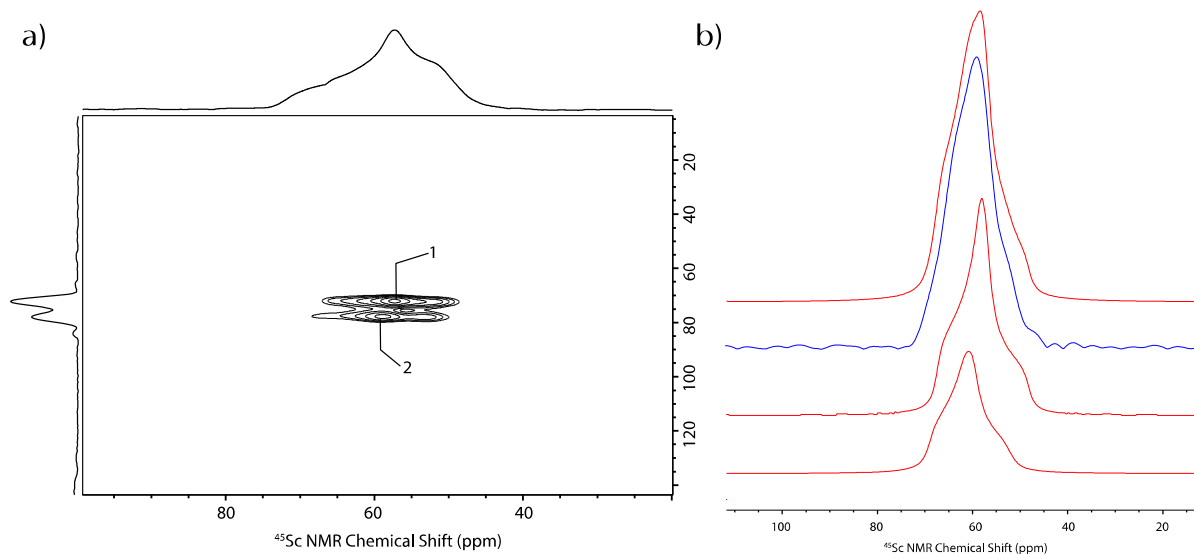
Results from this analysis are summarized in Table 3.

Figure 3. ^{45}Sc 3QMAS spectrum of Cp*$_2$ScCl(THF) (a) and simulation of 1D spin-echo ^{45}Sc MAS spectrum of Cp*$_2$ScCl(THF) containing two sites (b). Spectra were acquired at 14.1 T at 9 kHz spinning speed. Similar results were obtained at 9.4 T (see the Supporting Information).

Table 3. ^{45}Sc NMR Parameters for Cp*$_2$ScX(THF).

X	δ_{iso}	C_Q	η

	(ppm)	(MHz)	
F	12	26.0	0.1
Cl[a]	68	7.5	0.9
	71	7.3	0.8
Br[a]	99	7.2	0.4
	95	6.2	0.3
	69	7.9	0.3
	68	7.0	0.6
I[a]	132	7.5	0.3
	128	6.4	0.8

[a] – Values reported are averages obtained from fits at 14.1 T and 9.4 T.

DFT Calculations

The experimental data shows that the C_Q values of Cp*$_2$ScX(THF) are smaller than Cp*$_2$Sc–X. We performed DFT calculations to determine how structure and the Sc–X bond in these compounds influence C_Q. Geometry optimizations using B3LYP with Grimme's D3 dispersion with Becke-Johnson damping (GD3BJ)[16] functional at the SDD(Sc,X)/6-31(d,p) level

of theory closely reproduce the structures of Cp*$_2$Sc–X obtained experimentally. Key distances and angles of these optimized structures are summarized in the Supporting Information. The optimized structures of Cp*$_2$ScX(THF) are shown in Figure 4, and structural data is summarized in Table 4. All four complexes adopt bent metallocene geometries typical of d^0 metals. The Sc–Cp* bond distances are slightly longer and the and Cp*–Sc–Cp* bond angles are slightly smaller than the base-free halides. The Sc–X bond distances follow the expected order of Sc–F < Sc–Cl < Sc–Br < Sc–I and are only slightly longer than the Sc–X distances in the base free complexes.
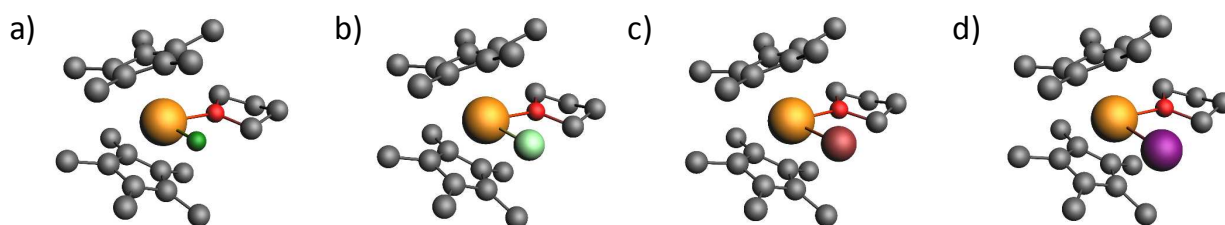

Figure 4. Optimized structures of Cp*$_2$ScF(THF) (a); Cp*$_2$ScCl(THF) (b); Cp*$_2$ScBr(THF) (c); Cp*$_2$ScI(THF) (d) at the B3LYP-GD3BJ/SDD(Sc,X)/6-31(d,p) level of theory in Gaussian 09.

Table 4. Selected Geometry Optimized Parameters for Cp*$_2$ScX(THF).

X	Cp*$_a$-Sc	Cp*$_b$-Sc	Cp*$_a$-Sc-Cp*$_b$	Sc-X	Sc-O	X-Sc-O
F	2.227 Å	2.227 Å	138.9°	1.931 Å	2.273 Å	83.7°
Cl	2.233 Å	2.234 Å	138.2°	2.475 Å	2.277 Å	87.7°
Br	2.233 Å	2.239 Å	137.5°	2.653 Å	2.286 Å	88.6°

| I | 2.237 Å | 2.245 Å | 137.4° | 2.910 Å | 2.293 Å | 89.2° |
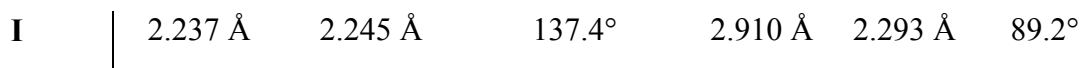
The calculated NMR parameters of Cp*$_2$Sc–X and Cp*$_2$ScX(THF) are given in Table 5. The predicted isotropic chemical shifts increase in the order F < Cl < Br < I and the C_Q values decrease in the order F > Cl > Br > I, which agrees with the trends observed experimentally. These calculations also predict the much smaller C_Q values for Cp*$_2$ScX(THF) than for base free Cp*$_2$Sc–X.

Table 5. Calculated ^{45}Sc NMR Parameters for Cp*$_2$ScX and for Cp*$_2$ScX(THF).

X	C_Q (MHz)	δ_{iso} (ppm)	η	Ω (ppm)	κ	α (°)	β (°)	γ (°)
F	-37.4	93	0.92	356	0.04	90	92	90
Cl	-30.8	207	0.17	316	0.17	90	91	90
Br	-29.5	224	0.13	255	0.26	82	91	91
I	-28.3	266	0.26	194	0.41	359	95	90
F(THF)	23.2	-30	0.10	139	-0.86	92	78	269
Cl(THF)	7.1	66	0.16	135	-0.43	28	95	92
Br(THF)	-5.9	83	0.20	122	0.04	150	89	265
I(THF)	-6.1	120	0.89	105	0.61	142	93	168

The orientation of the EFG tensor for Cp*$_2$Sc–F is shown in Figure 5a. The V_{33} of the EFG tensor, which determines the magnitude of C_Q (eq 1), is perpendicular to the Sc–F bond. This aligns V_{33} and the LUMO of Cp*$_2$Sc–F, which is shown in Figure 5b. The other halides have similar orientations that align V_{33} with their respective LUMO and are shown in Figure S26. The EFG tensor for Cp*$_2$ScF(THF) orients V_{33} nearly along the Sc–F bond (Figure 5c), and the LUMO is the π* combination from the lone pair of the fluoride and the scandium dz^2 (Figure 5d). The EFG tensor orientation of Cp*$_2$ScCl(THF) is similar. However, EFG tenors of

Cp*$_2$ScBr(THF) and Cp*$_2$ScI(THF) orient V$_{33}$ in similar directions as the base-free complexes. This orientation is shown in Figure 5e for the iodide. The calculated LUMO of Cp*$_2$ScI(THF), shown in Figure 5f, is the scandium dz^2 and shows negligible contributions from the p-orbital on the iodide.
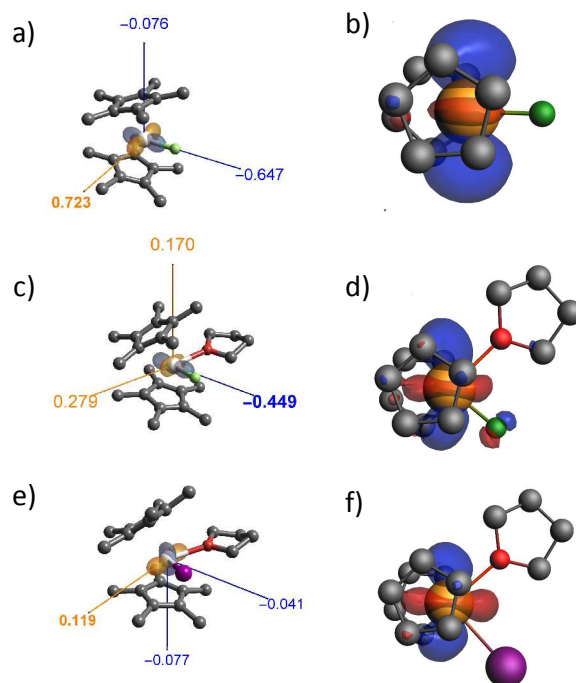

Figure 5. EFG Tensor plots of Cp*$_2$Sc–F (a), Cp*$_2$ScF(THF) (c), and Cp*$_2$ScI(THF) (e). LUMO of Cp*$_2$Sc–F (b), Cp*$_2$ScF(THF) (d), and Cp*$_2$ScI(THF) (f) calculated at B3LYP-GD3BJ/DZ; isovalue = 0.04.

Orbital decomposition analysis using DFT methods relates filled Natural Localized Molecular Orbitals (NLMO) to the magnitude of V$_{33}$.[25] Coupling between the EFG and the quadrupolar moment of the scandium nucleus is electric in origin, indicating that magnitude of V$_{33}$ will be related to core and valence orbitals. The results showing how various interactions in Cp*$_2$Sc–X affect V$_{33}$ are shown graphically in Figure 6a. The largest contributor to V$_{33}$ in

Cp*$_2$Sc–X are core scandium orbitals. The core halide orbitals become more significant contributors to V$_{33}$ moving down the halide series. The largest valence contribution to V$_{33}$ is the Sc–X σ-bond, decreasing in magnitude from fluoride to iodide. The two possible π-interactions in Cp*$_2$Sc–X, shown in Figures 6b and 6c for the fluoride, also contribute to V$_{33}$, though to a far smaller degree than the Sc–X σ-bonds.
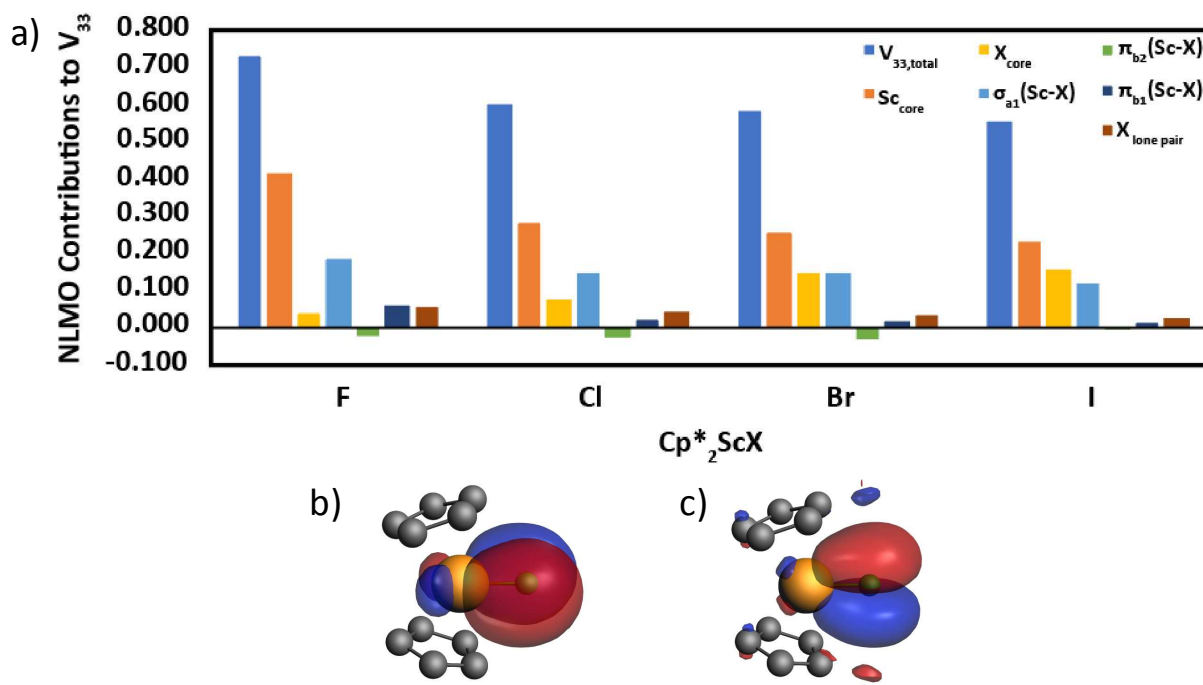

Figure 6. Contributions of NLMO to V$_{33}$ in Cp*$_2$Sc–X (a); π$_{b2}$ (b) and π$_{b1}$ (c) NLMO; isovalue = 0.01.

Analysis of V$_{33}$ for Cp*$_2$ScX(THF) is shown in Figure 7a. For clarity, the contributions from THF core and non-bonding orbitals are omitted from Figure 7a because these are minor contributors to V$_{33}$ and do not show obvious trends through the series. A table showing all contributions to V$_{33}$ for Cp*$_2$ScX(THF) is given in the Supporting Information. The core scandium and halide orbitals follow similar trends as found in the base-free halides, though these

contributions become nearly negligible for the chloride, bromide, and iodide. The four valence orbitals that affect V_{33} are shown for the fluoride in Figure 7b–e. These orbitals are the σ/π bonding pairs expected for a d^0 $Cp_2MX(L)$ fragment (Figure 7b and 7c) and two π-interactions between empty scandium orbitals and the appropriate orbtials on the halide (Figure 7d and 7e). The σ/π bonding network contributes greater magnitudes to V_{33} than the π-interactions, similar to that observed in the base-free halides. In general, the magnitudes of the contribution to V_{33} for a given valence NLMO follows the trend F > Cl > Br > I.
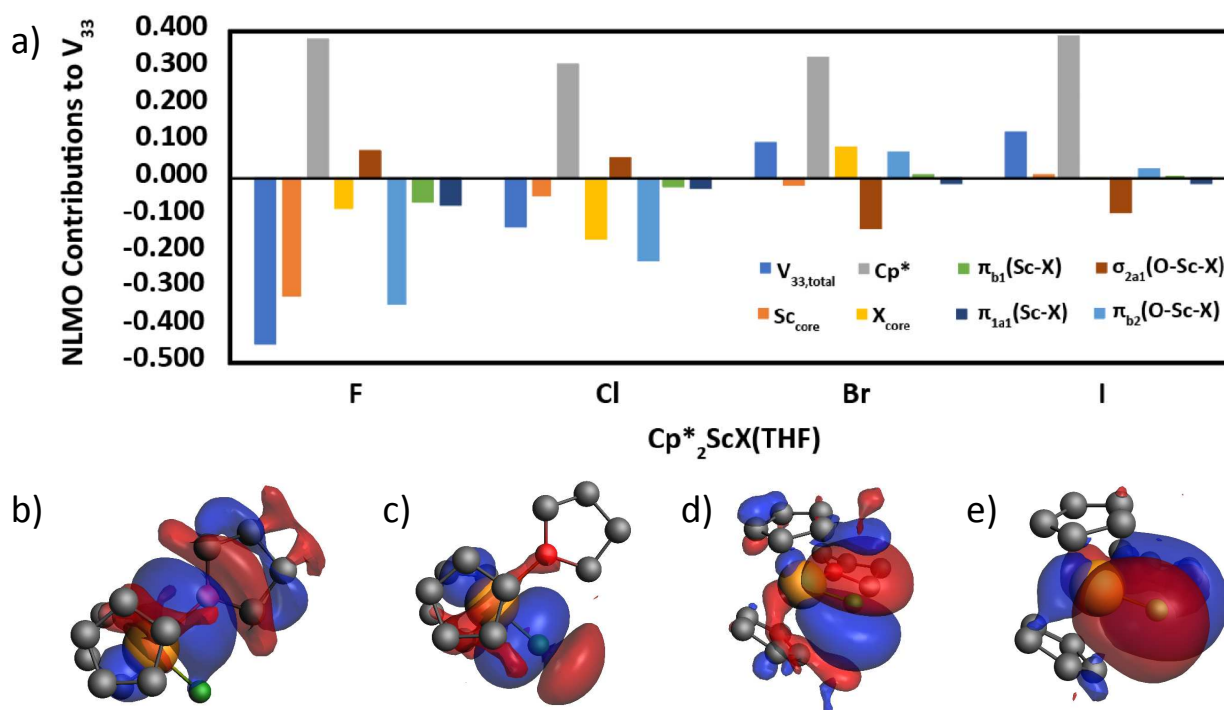

Figure 7. Contributions of NLMO to V_{33} in $Cp*_2ScX(THF)$ (a); plots of valence NLMO σ_{1a1} (b), π_{b2} (c), π_{b1} (d) and π_{2a1} (e) for the fluoride; isovalue = 0.005.

Discussion

The base-free halides of Cp*$_2$Sc–X are readily prepared by straightforward synthetic procedures. The solid-state structures of these compounds show that the Sc–X bond distance follows trends that are typical of early metallocene complexes. The solid-state ^{45}Sc NMR properties of the base-free halides show that the fluoride has the largest C_Q and iodide has the smallest C_Q. Based on quadrupolar NMR studies of BX$_3$ (X = halide)[26] and organoaluminum compounds,[27] this behavior could be related to the degree of π-bonding in the Sc–X bond. However, DFT results show that several electronic parameters in the Sc–X bond affect C_Q. The largest contributors to C_Q in this series are core contributions from filled 2p and 3p Sc core orbitals, decreasing from fluoride to iodide, and filled halide core orbitals, which increase from fluoride to iodide. Filled core orbital subshells have spherical symmetry and should not contribute to V_{33}. The DFT analysis above includes nuclear charge contributions to EFG. Nonzero contributions to C_Q from core orbitals are related to the incomplete shielding of nuclear charge by outer core orbitals from bonding partners and polarizability.[11a] The filled core scandium orbitals decrease contributions to V_{33} from fluoride to iodide because the Sc–X distance increases moving down the series. This relationship is a result of Sternheimer shielding,[28] which relates the polarization of core electrons by valence orbitals and is dependent on the distance between bonding partners. The halide core contributions follow the opposite trend because halides become more polarizable moving down the halide series. The Sc–X σ–bonds also contribute to C_Q, but less than core contributions, and the π-interactions are nearly negligible contributors to V_{33}.

Cp*$_2$Sc–X react with THF to form adducts that, in our hands, do not form single crystals. DFT calculations show that Cp*$_2$ScX(THF) adopt pseudotetrahedral geometries at Sc typical of d^0 bent metallocenes. This increase in spherical symmetry is expected to result in smaller C_Q

values than the planar base-free halides. Coordination of THF to the base-free halide also has

consequences related to the orientation of V_{33} that relate to the qualitative molecular orbitals in

Cp*$_2$ScX(THF).

The qualitative molecular orbitals in Cp*$_2$Sc–X and Cp*$_2$ScX(THF) using the Dahl-

Petersen axis system[29] are shown in Figure 8. Cp*$_2$Sc–X contains one σ-ScX ($2a_1$) and two π-

ScX (b_1 and b_2) interactions. The LUMO in Cp*$_2$Sc–X is the $1a_1$ dz^2 orbital. Bonding in

Cp*$_2$ScX(THF) is similar. The σ-ScX(THF) ($2a_1$) and π-ScX(THF) (b_1 and b_2) bonds are formed

between scandium and C_{2v} fragment orbitals.[30] The noticeable difference in bonding between

Cp*$_2$Sc–X and Cp*$_2$ScX(THF) is possibility to form a third π-ScX ($1a_1$) bond in the latter family

of complexes.
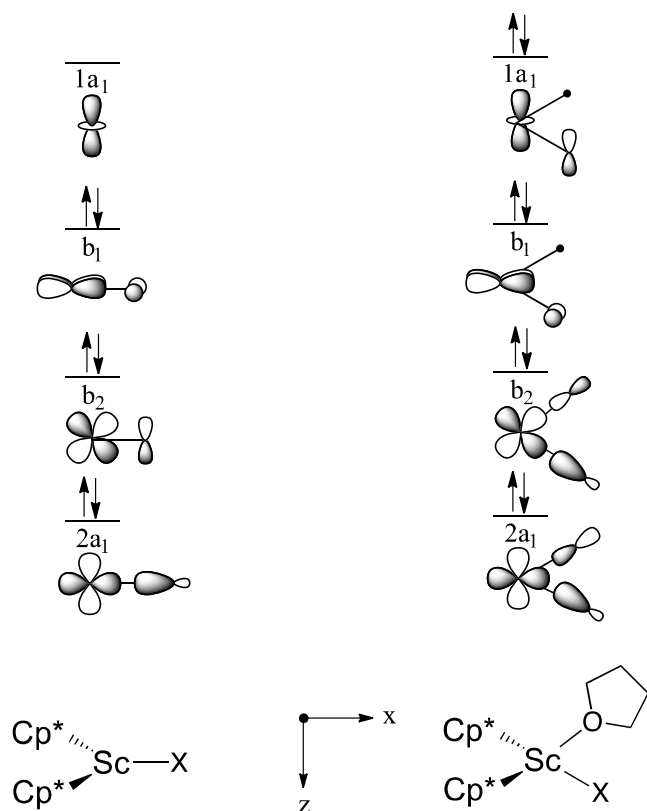
Figure 8. Qualitative molecular orbitals in Cp*$_2$Sc–X (left) and Cp*$_2$ScX(THF) (right).

DFT calculations connect this bonding picture to the ^{45}Sc NMR studies described above. The magnitude of the V_{33} component of the EFG tensor, which determines C_Q, in Cp*$_2$Sc–X aligns with the dz^2 LUMO. This co-alignment of the LUMO in Cp*$_2$Sc–X and V_{33} is a consequence of semi-empirical studies by Townes and Dailey[21] relating the magnitude of C_Q to the population of empty orbitals. Therefore, occupation of the dz^2 LUMO in Cp*$_2$Sc–X is expected to reduce the C_Q. In the THF adducts, the b$_2$ π-orbital that forms the σ-ScX bond is a large contributor to V_{33}, and the 2a$_1$ dz^2 orbital that is empty in Cp*$_2$Sc–X engages in a π-interaction with a lone pair on X. The 1a$_1$ orbital contribution to V_{33} following the trend F > Cl > Br > I, similar to the spectroelectrochemical trend found for Cp*$_2$Ti–X.

Conclusions

The halides of Cp*$_2$Sc–X and Cp*$_2$ScX(THF) were studied by solid-state ^{45}Sc NMR spectroscopy and DFT methods. These studies showed that C_Q, a sensitive reporter of electronic structure, is related to core orbitals on scandium and the halide for the base free adducts, which is related to Sc–X bond distance and polarizability of the halide. In Cp*$_2$Sc–X, the Sc–X π-bonds contribute small relative magnitudes to V_{33} across the halide series, indicating that C_Q does not provide a measure of π-donation to scandium for the base-free compounds. Including an extra ligand, as in Cp*$_2$ScX(THF) results in smaller C_Q values than observed in the base-free adducts. Although core contributions are also relevant in this family of compounds, σ/π bonding interactions are more pronounced in their contributions to V_{33} and follow similar trends to those found for Cp*$_2$Ti–X from UV-vis and EPR studies. These results show that analysis of C_Q for scandocene complexes provides valuable electronic and structural information.

Acknowledgements

References

(1) a) Thompson, M. E.; Baxter, S. M.; Bulls, A. R.; Burger, B. J.; Nolan, M. C.; Santarsiero, B. D.; Schaefer, W. P.; Bercaw, J. E. *J. Am. Chem. Soc.* **1987**, *109*, 203-219; b) Waterman, R. *Organometallics* **2013**, *32*, 7249-7263.
(2) Sadow, A. D.; Tilley, T. D. *J. Am. Chem. Soc.* **2003**, *125*, 7971-7977.
(3) a) Hayes, P. G.; Piers, W. E.; McDonald, R. *J. Am. Chem. Soc.* **2002**, *124*, 2132-2133; b) Zeimentz, P. M.; Arndt, S.; Elvidge, B. R.; Okuda, J. *Chem. Rev.* **2006**, *106*, 2404-2433; c) Nishiura, M.; Guo, F.; Hou, Z. M. *Acc. Chem. Res.* **2015**, *48*, 2209-2220; d) Chen, J. Z.; Gao, Y. S.; Wang, B. H.; Lohr, T. L.; Marks, T. J. *Angew. Chem. Int. Ed.* **2017**, *56*, 15964-15968.
(4) Berkefeld, A.; Piers, W. E.; Parvez, M.; Castro, L.; Maron, L.; Eisenstein, O. *J. Am. Chem. Soc.* **2012**, *134*, 10843-10851.
(5) LeBlanc, F. A.; Piers, W. E.; Parvez, M. *Angew. Chem. Int. Ed.* **2014**, *53*, 789-792.
(6) Rossini, A. J.; Schurko, R. W. *J. Am. Chem. Soc.* **2006**, *128*, 10391-10402.
(7) Giovine, R.; Volkringer, C.; Ashbrook, S. E.; Trébosc, J.; McKay, D.; Loiseau, T.; Amoureux, J.-P.; Lafon, O.; Pourpoint, F. *Chem. Eur. J.* **2017**, *23*, 9525-9534.
(8) Alba, M. D.; Chain, P.; Florian, P.; Massiot, D. *J. Phys. Chem. C* **2010**, *114*, 12125-12132.
(9) Vancompernolle, T.; Trivelli, X.; Delevoye, L.; Pourpoint, F.; Gauvin, R. M. *Dalton Trans.* **2017**, *46*, 13176-13179.
(10) Culver, D.; Huynh, W.; Tafazolian, H.; Ong, T. C.; Conley, M. P. *Angew. Chem. Int. Ed.*, **2018**, *57*, 9520-9523.
(11) a) Autschbach, J.; Zheng, S.; Schurko, R. W. *Conc. Mag. Res. A* **2010**, *36A*, 84-126; b) Ashbrook, S. E.; Sneddon, S. *J. Am. Chem. Soc.* **2014**, *136*, 15440-15456; c) Monika, S.; Jochen, A. *Chem. Eur. J.* **2013**, *19*, 12018-12033.
(12) Lukens, W. W.; Smith, M. R.; Andersen, R. A. *J. Am. Chem. Soc.* **1996**, *118*, 1719-1728.
(13) Medek, A.; Frydman, V.; Frydman, L. *J. Phys. Chem. A* **1999**, *103*, 4830-4835.
(14) Amoureux, J.-P.; Fernandez, C.; Steuernagel, S. *J. Mag. Res. A* **1996**, *123*, 116-118.

(15) Gaussian 09, R. E. M. J. F., G. W. Trucks, H. B. Schlegel, G. E. Scuseria, M. A. Robb, J. R. Cheeseman, G. Scalmani, V. Barone, G. A. Petersson, H. Nakatsuji, X. Li, M. Caricato, A. Marenich, J. Bloino, B. G. Janesko, R. Gomperts, B. Mennucci, H. P. Hratchian, J. V. Ortiz, A. F. Izmaylov, J. L. Sonnenberg, D. Williams-Young, F. Ding, F. Lipparini, F. Egidi, J. Goings, B. Peng, A. Petrone, T. Henderson, D. Ranasinghe, V. G. Zakrzewski, J. Gao, N. Rega, G. Zheng, W. Liang, M. Hada, M. Ehara, K. Toyota, R. Fukuda, J. Hasegawa, M. Ishida, T. Nakajima, Y. Honda, O. Kitao, H. Nakai, T. Vreven, K. Throssell, J. A. Montgomery, Jr., J. E. Peralta, F. Ogliaro, M. Bearpark, J. J. Heyd, E. Brothers, K. N. Kudin, V. N. Staroverov, T. Keith, R. Kobayashi, J. Normand, K. Raghavachari, A. Rendell, J. C. Burant, S. S. Iyengar, J. Tomasi, M. Cossi, J. M. Millam, M. Klene, C. Adamo, R. Cammi, J. W. Ochterski, R. L. Martin, K. Morokuma, O. Farkas, J. B. Foresman, and D. J. Fox, 2016.
(16) Stefan, G.; Stephan, E.; Lars, G. *J. Comput. Chem.* **2011**, *32*, 1456-1465.
(17) T. H. Dunning Jr. and P. J. Hay, Mondern Theoretical Chemistry, Ed. H. F. Schaefer III, Vol. 3 (Plenum, New York, 1977) 1-28.
(18) Velde, G.; Bickelhaupt, F. M.; Baerends, E. J.; Guerra, C. F.; Van Gisbergen, S. J. A.; Snijders, J. G.; Ziegler, T. *J Comput Chem* **2001**, *22*, 931-967; b) Guerra, C. F.; Snijders, J. G.; te Velde, G.; Baerends, E. J. *Theor Chem Acc* **1998**, *99*, 391-403.
(19) a) Schreckenbach, G.; Ziegler, T. *J Phys Chem.* **1995**, *99*, 606-611; b) Krykunov, M.; Ziegler, T.; Van Lenthe, E. *Int J Quantum Chem* **2009**, *109*, 1676-1683.
(20) a) van Lenthe, E.; Baerends, E. J; Snijders, J. G. *J. Chem. Phys.* **1996**, *105*, 6505-6516; b) van Lenthe, E.; Baerends, E. J; Snijders, J. G. *J. Chem. Phys.* **1994**, *101*, 9783-9792; c) van Lenthe, E.; Baerends, E. J; Snijders, J. G. *J. Chem. Phys.* **1993**, *99*, 4597-4610.

(21) a) Vanlenthe, E.; Baerends, E. J.; Snijders, J. G. *J Chem Phys* **1993**, *99*, 4597-4610; b) Vanlenthe, E.; Baerends, E. J.; Snijders, J. G. Relativistic *J Chem Phys* **1994**, *101*, 9783-9792.
(22) Rudolph, W. W.; Pye, C. C. *J. Phys. Chem. A* **2000**, *104*, 1627-1639.
(23) a) Strazisar, S. A.; Wolczanski, P. T. *J. Am. Chem. Soc.* **2001**, *123*, 4728-4740; b) Wada, S.; Jordan, R. F. *Angew. Chem. Int. Ed.* **2017**, *56*, 1820-1824; c) Foley, S. R.; Stockland, R. A.; Shen, H.; Jordan, R. F. *J. Am. Chem. Soc.* **2003**, *125*, 4350-4361; d) Stockland, R. A.; Foley, S. R.; Jordan, R. F. *J. Am. Chem. Soc.* **2003**, *125*, 796-809; e) Stockland, R. A.; Jordan, R. F. *J. Am. Chem. Soc.* **2000**, *122*, 6315-6316; f) Kilyanek, S. M.; Stoebenau, E. J.; Vinayavekhin, N.; Jordan, R. F. *Organometallics* **2010**, *29*, 1750-1760; g) Shen, H.; Jordan, R. F. *Organometallics* **2003**, *22*, 2080-2086.
(24) Medek, A.; Harwood, J. S.; Frydman, L. *J. Am. Chem. Soc.* **1995**, *117*, 12779-12787.
(25) Rossini, A. J.; Mills, R. W.; Briscoe, G. A.; Norton, E. L.; Geier, S. J.; Hung, I.; Zheng, S.; Autschbach, J.; Schurko, R. W. *J. Am. Chem. Soc.* **2009**, *131*, 3317-3330.
(26) Das, T. P. *J. Chem. Phys.* **1957**, *27*, 1-10.
(27) Tang, J. A.; Masuda, J. D.; Boyle, T. J.; Schurko, R. W. *ChemPhysChem* **2006**, *7*, 117-130.
(28) Lucken, E. A. C.: *Nuclear quadrupole coupling constants*; Academic P., 1969.
(29) Petersen, J. L.; Dahl, L. F. *J. Am. Chem. Soc.* **1975**, *97*, 6416-6422.
(30) Albright, T. A.; Burdett, J. K.; Whangbo, M. H.: *Orbital Interactions in Chemistry*; Wiley, 2013.

TOC Graphic
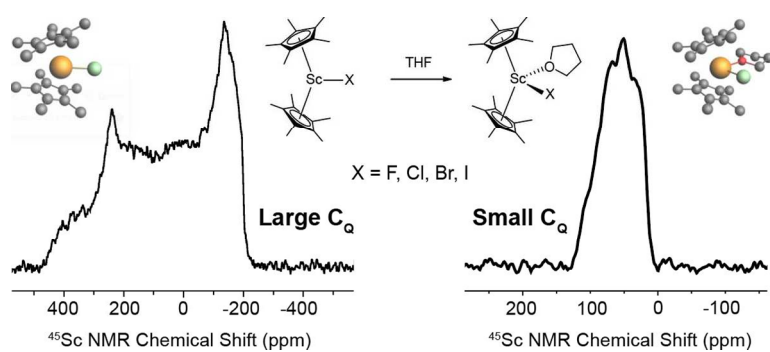
A systematic study showing how the Sc–X bond affects solid-state ^{45}Sc NMR quadrupolar coupling constants in Cp*$_2$Sc–X.